ADVANCED ENERGY MATERIALS
www.advenergymat.de

Organic Bilayer Photovoltaics for Efficient Indoor Light Harvesting

*Song Yi Park, Chiara Labanti, Joel Luke, Yi-Chun Chin, and Ji-Seon Kim**

Indoor organic photovoltaics (OPVs) are a potential niche application for organic semiconductors due to their strong and well-matched absorption with the emission of indoor lighting. However, due to extremely low photocurrent generation, the device parameters critical for efficient indoor OPVs differ from those under 1 Sun conditions. Herein, these critical device parameters—recombination loss and shunt resistance (R_{sh})—are identified and it is demonstrated that bilayer OPVs are suitable for indoor PV applications. Compared to bulk-heterojunction (BHJ), the open-circuit voltage loss of bilayer devices under low light intensities is much smaller, consistent with a larger surface photovoltage response, indicating suppressed recombination losses. The bilayer devices show a higher fill factor at low light intensities, resulting from high R_{sh} afforded by the ideal interfacial contacts between the photoactive and the charge transport layers. The high R_{sh} enables bilayer devices to perform well without a light-soaking process. Finally, the charge carriers are extracted rapidly in bilayers, which are attributed to strongly suppressed trap states possibly induced by isolated domains and non-ideal interfacial contacts in BHJs. This study highlights the excellent suitability of bilayer OPVs for indoor applications and demonstrates the importance of device architecture and interfacial structures for efficient indoor OPVs.

1. Introduction

With the recent fast development of non-fullerene acceptors (NFAs), power conversion efficiencies (PCEs) of organic photovoltaic (OPV) cells now exceed 18% under 1 Sun (AM1.5G) excitation conditions.[1] With an increasing number of these high PCE reports, research interest is moving toward implementing OPVs in practical applications, which include transparent devices,[2] colorful semi-transparent devices,[3] and devices for indoor photovoltaics.[4–7] Indoor light harvesting applications have especially attracted great attention as the demand for low-power electronic devices is increasing rapidly with the advent of the Internet of Things, radio-frequency identification, Bluetooth low energy, etc. requiring ≈10 µW to ≈1 mW of electrical power to communicate between wireless electronic devices.[8]

Indoor OPVs utilize organic semiconductors as the photoactive material in indoor energy harvesting devices. This allows for optical band gap control to ensure a good match with the visible emission spectra (300–800 nm) of indoor lighting, such as light emitting diodes (LEDs), fluorescent lamps, or halogen lamps.[7,9] Freunek et al. reported theoretical maximum PCE limits of photovoltaic devices under indoor lighting conditions as a function of optical band gap of photoactive materials.[10] In case of white RGB LEDs, for example, theoretical maximum PCE limits of over 50% can be achieved when a photoactive material with an optical band gap of 1.90 eV is used. This emphasizes the importance of the spectral overlap to achieve high PCEs in indoor photovoltaics, exemplifying the applicability of OPVs to indoor applications. Additional to the optical band gap, the frontier molecular orbital energy levels of organic semiconductors can be controlled by adjusting molecular structure. Therefore, unlike inorganic photovoltaic devices, both a high short-circuit current density (J_{SC}) and open-circuit voltage (V_{OC}) can be achieved. Although promising, there are some important considerations when using OPVs for indoor light applications. For example, unlike use under solar radiation (1 Sun), typical light intensities of indoor conditions (e.g., office, supermarket, etc.) are very low, ≈1000 lux. Due to the low light intensity, the photocurrent density of OPVs is also extremely low, typically around hundreds of µA cm^{-2}. Therefore, minimizing leakage currents and reducing recombination losses are essential strategies to achieve highly efficient indoor OPVs.[5,6,11,12]

Most research related to indoor OPVs utilizes a bulk-heterojunction (BHJ) photoactive layer. BHJs have been widely used to overcome the limitations of organic semiconductors, namely a large exciton binding energy, and short exciton diffusion lengths (L_D).[13] Randomly intermixed donor and acceptor domains in BHJs facilitate exciton dissociation at the interface between donor and acceptor, leading to high photocurrent generation. However, this nano-structured morphology can induce unwanted energy losses by trapped charge carriers

S. Y. Park, C. Labanti, J. Luke, Y.-C. Chin, J.-S. Kim
Department of Physics and Centre for Processable Electronics
Imperial College London
London SW7 2AZ, UK
E-mail: ji-seon.kim@imperial.ac.uk

The ORCID identification number(s) for the author(s) of this article can be found under https://doi.org/10.1002/aenm.202103237.

DOI: 10.1002/aenm.202103237

in isolated domains or non-ideal interfaces in which there is physical contact between the donor and electron transport layer (ETL) or the acceptor and hole transport layer (HTL). To overcome this limitation and enhance device performance further, pseudo bilayer (p-i-n structure) strategies have been suggested recently. Sequential deposition method provides p-i-n structures with certain degree of interdiffusion of top layer into bottom layer, resulting in higher concentration gradient of acceptors near the cathode and donors near the anode. This strategy enhances device performance further compared to conventional BHJ devices, with slightly mitigated trap-assisted recombination losses.[14] A bilayer-heterojunction which has relatively clearer donor/acceptor interfaces than those of p-i-n structure is another potential candidate to overcome the morphological limitations of BHJs. Recently high PCEs (10–11%) have been reported using polymer/NFA bilayers, achieved by efficient long-range energy transfer and long L_D >30 nm.[15,16] Lee et al. demonstrate a reduction of non-radiative V_{OC} losses and suppressed trap-assisted recombination in bilayer devices compared with BHJs. These properties can partially compensate the loss of charge generation in thinner layers, resulting in similar or slightly better device performance than BHJ devices.[17] Based on this previous research, we consider trap sites can be introduced inevitably by the intrinsic nature of BHJ structure.

Under 1 Sun intensity, the effect of trap-assisted recombination in BHJs is often very minor, and may not limit device performance significantly. However, it might be a serious problem at indoor light conditions due to a much lower density of generated charge carriers. Indeed, recent report demonstrated suppression of trap states via a diluting strategy with insulating polystyrene enables to achieve efficient ultra-thick indoor OPV devices.[18] Therefore, it is important to identify the device parameters critical for indoor applications and furthermore to clarify whether the BHJ or the bilayer is more suitable as the photoactive layer structure under indoor light conditions. Although efficient bilayer OPV results have been reported recently, their application to indoor light conditions have not been explored so far.

In this work, we report a detailed comparison of BHJ and bilayer OPVs under different measurement conditions of 1 Sun and indoor lighting (1000 lux, white LED) to investigate the differences in device behavior as illustrated in **Figure 1**a. Under 1 Sun, BHJ devices exhibit better OPV performance compared to bilayer devices. However, under indoor light conditions, this trend is reversed—with the maximum power output (P_{max}) of bilayer devices being higher than that of BHJ OPVs. The considerable P_{max} drop of BHJ under indoor light is mainly due to a significant drop in V_{OC}. Bilayer devices, on the other hand, exhibit a much smaller drop of V_{OC} and a significant increase in FF, which leads to the higher P_{max} under indoor light. Furthermore, light soaking (LS) with 1 Sun excitation prior to indoor light operation is not essential for bilayer devices, whereas BHJ devices require LS to obtain high efficiency. Bilayer devices have sufficiently high shunt resistance (R_{sh}) even without LS, originating from more ideal interfacial contacts formed in bilayers (i.e., pure donor layer next to HTL and pure acceptor layer next ETL), unlike in BHJs. Finally, we demonstrate high performance bilayer devices under indoor light, which show suppressed trap states and efficient charge extraction. This study highlights the importance of device architecture and morphological properties of OPVs for efficient indoor light harvesting and suggests the great potential of bilayer OPVs for indoor photovoltaic applications.

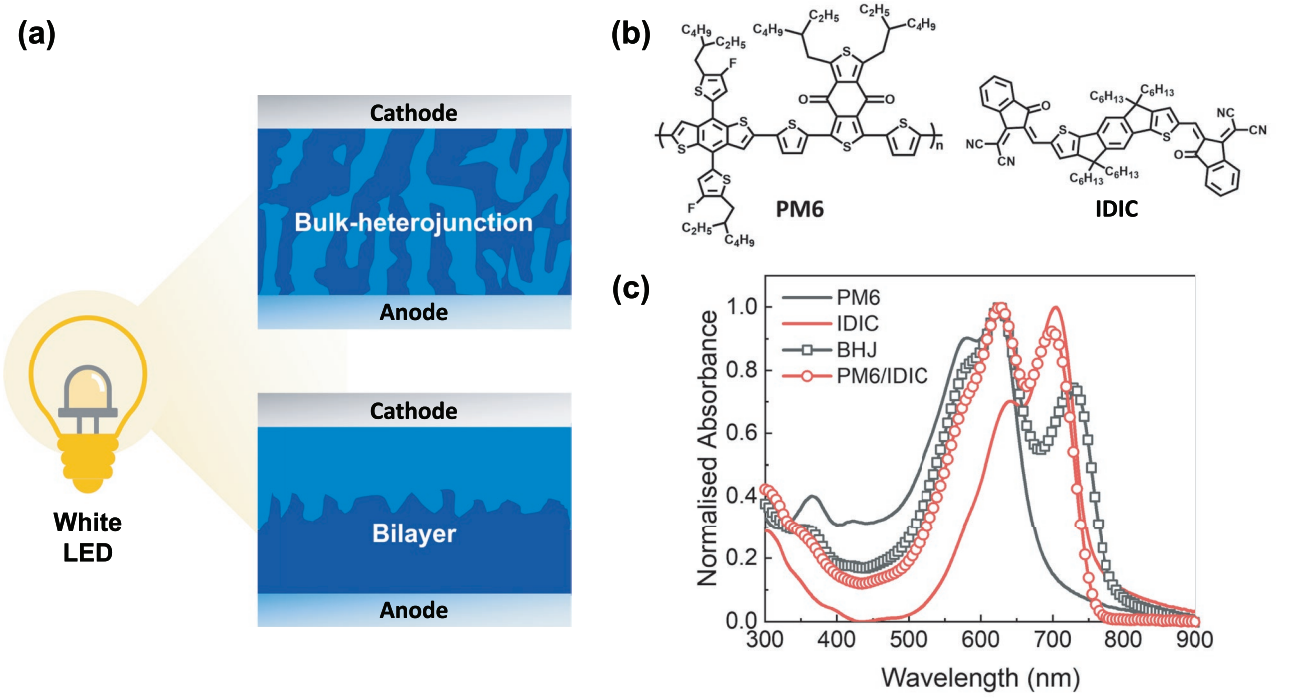

Figure 1. a) Illustration of BHJ and bilayer OPV devices with indoor white LED. b) Molecular structure of PM6 as a donor and IDIC as an acceptor. c) Normalized absorption spectra of PM6 (60 nm), IDIC (82 nm), BHJ (123 nm) and bilayer (D/A 60/82 nm) films.

2. Results and Discussion

2.1. Device Configuration and Material Properties

BHJ and bilayer devices were fabricated in a conventional structure, with detailed fabrication procedures in the Supporting Information. The devices were measured under 1 Sun using a solar simulator and under indoor light using a white LED, whose emission spectrum is shown in Figure S1, Supporting Information. Commercially available PM6[19] and IDIC[20] (Figure 1b, molecular structure) were selected as donor and acceptor for the photoactive layer, respectively. These materials are chosen due to their long exciton diffusion lengths of 35.8 nm for PM6 and 35 nm for IDIC, and efficient long-range energy transfer from donor to acceptor suitable for bilayer devices.[16] Bilayer films were prepared by depositing the NFA on top of the polymer layer using an orthogonal solvent (dichloromethane (DCM)) which selectively dissolves NFAs but not polymers. We first confirm the PM6/IDIC bilayer structure by directly probing the energy levels of the top and bottom layers using ambient photoemission spectroscopy (APS). APS is a useful tool to determine the energetics of organic semiconductors, particularly their highest occupied molecular orbital, by finding the onset of photoemission upon photoexcitation.[21] PM6 (60 nm), IDIC (50 nm), BHJ (120 nm), and bilayer (PM6/IDIC 60/50 nm) films were prepared on ITO substrates and their photoemission spectra were compared as shown in Figure S2, Supporting Information. APS detects the photoemission signal near the surface of the organic semiconductor films. Thus, if the bilayer is well formed, the photoemission spectrum of the top IDIC layer should be similar or the same as a neat IDIC film. As expected, the photoemission spectrum of the bilayer sample is almost the same as neat IDIC film, whereas in the BHJ film there is a significant difference between neat and blend films, confirming the well-formed PM6/IDIC bilayer structure, as confirmed elsewhere by other characterization tools.[15,16]

Figure 1c presents UV–Vis absorption spectra of PM6, IDIC, BHJ, and bilayer films. BHJ films show a slightly red-shifted absorption of the IDIC absorption peak (730 nm) relative to the neat film (706 nm). This is due to IDIC aggregation upon thermal annealing of the BHJ film (Figure S3, Supporting Information). Also, slower evaporation of chlorobenzene (host solvent for BHJs) can accelerate IDIC aggregation further compared to DCM (host solvent for IDIC in bilayers), which is consistent with red-shifted absorption spectra of neat IDIC films (Figure S4, Supporting Information). The absorption spectrum of bilayer films is well matched with both neat PM6 and IDIC absorbance. More crystallized IDIC molecules in BHJs might be beneficial in terms of low-energy light absorption and electron transport properties, but it does not contribute to photocurrent generation especially in case of indoor light illumination, due to lack of spectral overlap with the white LED source which will be discussed in the next section.

2.2. Device Characterization under 1 Sun and Indoor Light

First, we investigate the optimum bilayer OPV devices under indoor light conditions. For this, donor and acceptor thicknesses were varied to give PM6/IDIC devices with thicknesses of 93/50, 60/50, 60/72 and 60/103 nm. The devices were characterized under both 1 Sun and indoor light conditions (1000 and 500 lux) (Figure S5 and Table S1, Supporting Information). Unbalanced thickness conditions of 93/50 and 60/103 nm for PM6/IDIC bilayers showed poor device performance regardless of light intensity, indicating the importance of balanced charge transport in obtaining good device performance not only for 1 Sun, but also indoor light conditions. In case of relatively balanced thicknesses, namely 60/50 and 60/72 nm PM6/IDIC devices, the slightly thicker IDIC devices (60/72 nm) showed better OPV performance under indoor light conditions, particularly due to an enhanced fill factor (FF). This could originate from the different morphological properties of the bilayer stacks. Surface morphologies measured by atomic force microscopy (AFM) of thin- and thick-IDIC bilayers (40 and 82 nm, respectively) are totally different (Figure S6, Supporting Information). The surface morphology of the thin-IDIC top layer is strongly affected by surface roughness of the PM6 bottom layer. However, the thick-IDIC top layer shows more aggregated features, similar to neat IDIC, indicating that the top of the thicker layer is less affected by PM6 surface roughness. This aggregated IDIC can be beneficial for device performance since electron transport and extraction to the ETL can be much faster through the aggregated IDIC layer. Absorption spectra are also consistent with AFM results. In thin-IDIC bilayers, absorbance at longer wavelengths was slightly blue-shifted and intensity lowered compared to neat IDIC films (Figure S7a, Supporting Information), which can be attributed to inhibited aggregation of IDIC due to the rough surface of the PM6 bottom layer. However, in the thick-IDIC bilayer, the main absorption peaks at 637 and 701 nm were well matched with that of neat PM6 and neat IDIC, respectively, with increased intensity of absorbance at longer wavelengths as shown in Figure 1c. These data demonstrate the sensitivity of indoor light performance to the morphology of each donor and acceptor layer within the bilayer structure and the important role played by thickness in device optimization.

Next, based on optimized device structures, we investigate the impact of the photoactive layer structure (BHJ vs bilayer) and its morphological properties on indoor OPV performance. We compared device performance of BHJ and bilayer under 1 Sun and 1000 lux (white LED) illumination. BHJ devices were optimized by varying the photoactive layer thickness, the solvents used for deposition and the thermal annealing conditions (Table S2, Supporting Information), and optimum BHJ devices were used for comparison with bilayers. Representative current density–voltage (*J*–*V*) curves of optimum devices are shown in **Figure 2**a,b and corresponding photovoltaic parameters are summarized in **Table 1**. Under 1 Sun, BHJ devices showed better OPV performance with higher J_{SC} and FF, but slightly lower V_{OC} compared to bilayer devices. This result is expected since the extremely large interfacial areas between donor and acceptor can lead to efficient charge generation producing high photocurrent in BHJ devices. However, the lower V_{OC} is possibly due to higher recombination losses induced by the intermixed BHJ morphology, resulting in charge trapping in isolated domains or buried interfaces.[17,22] In contrast, under indoor light conditions the trend of device performances of BHJ and bilayer devices is reversed—bilayer devices showed similar J_{SC}, but much higher V_{OC} and FF (Figure 2b). Consequently, bilayer devices showed a higher P_{max}

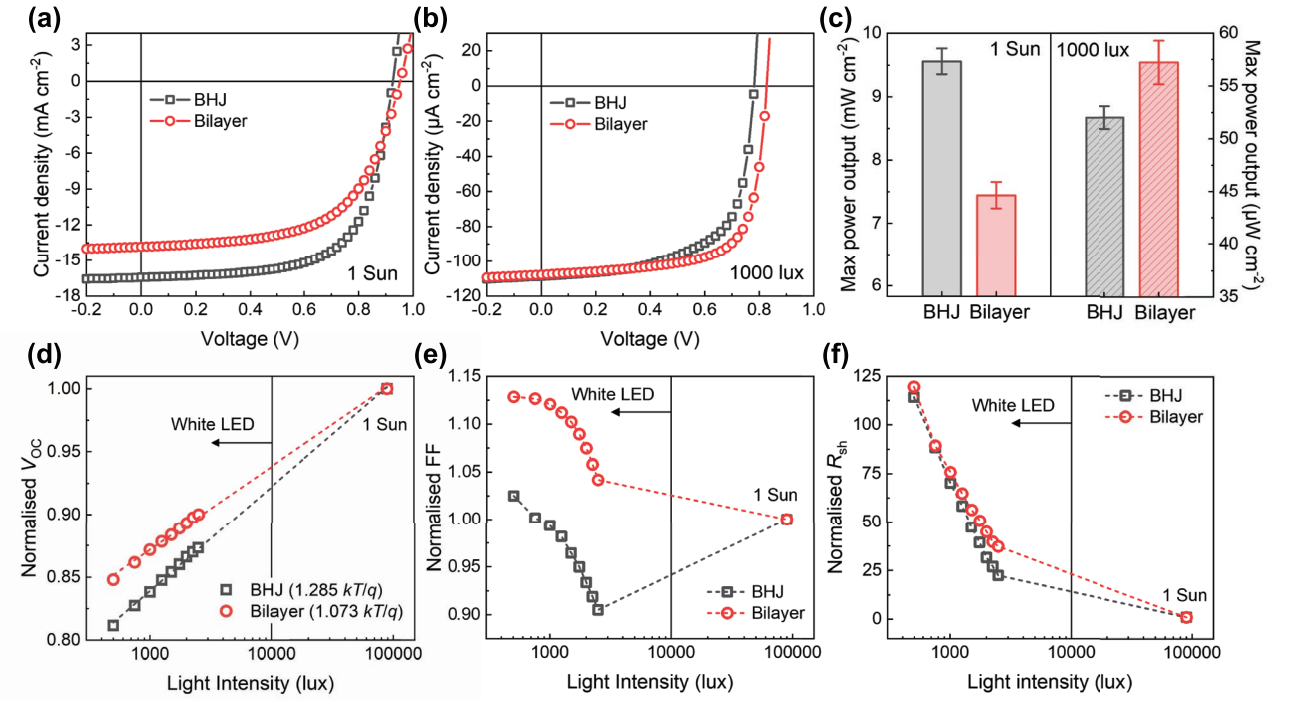

Figure 2. a,b) Representative *J–V* curves of optimum BHJ and bilayer OPV devices, measured under 1 Sun (solar simulator) and 1000 lux (white LED), respectively. c) Summary of maximum power output values averaged from 10 devices. Light intensity dependence on d) V_{OC}, e) FF, and f) R_{sh} of the BHJ and bilayer devices with normalization at 1 Sun. Note that V_{OC} and FF were averaged from 10 devices, and R_{sh} was averaged from 3 devices.

of 62.6 μW cm^{-2} than that of BHJ devices (P_{max} = 54.6 μW cm^{-2}) under 1000 lux illumination (Figure 2c). Due to extremely low photocurrent generation under indoor light conditions, leakage currents can affect device performance significantly, which is less critical under 1 Sun illumination. To confirm whether the indoor-light power density difference is originated from the leakage current difference, we measured dark *J–V* curves (Figure S8, Supporting Information). Both BHJ and bilayer devices showed similarly low leakage currents, indicating that this cannot account for the differences in device behavior.

2.3. Light-Intensity Dependent Photovoltaic Parameters and Shunt Resistance

Under indoor light, the main improved parameters in bilayer devices compared to the BHJ are V_{OC} and FF. To understand these improvements in detail, we investigate light intensity dependence on V_{OC}, FF, R_{sh} and plot them normalized to 1 Sun, as shown in Figure 2d–f. Plots without normalization and corresponding *J–V* curves are shown in Figures S9 and S10, respectively, Supporting Information, and corresponding PV parameters are summarized in Table S3, Supporting Information. The intensity-dependent measurement was conducted with a sequence of low (500 lux) to high (2500 lux) intensity of indoor light, followed by 1 Sun (90 000 lux) measurement.

From light-intensity dependence on V_{OC}, information about trap-assisted recombination can be obtained. When bimolecular recombination is the only loss mechanism in a given system, the slope of V_{OC} versus the natural logarithm of light intensity is kT/q. If the slope is greater than kT/q, it indicates that trap-assisted recombination is competing with bimolecular recombination, showing stronger dependence of V_{OC} on light intensity.[23] We calculated the slopes for both BHJ and bilayer

Table 1. Summary of photovoltaic parameters of BHJ and bilayer OPV devices, measured under 1 Sun and 1000 lux (white LED). All parameters were averaged from 10 devices.

Light intensity	Active layer	J_{SC} [mA cm^{-2}]	V_{OC} [V]	FF	PCE [%]	Best PCE [%]
1 Sun	BHJ	16.3 ± 0.29	0.922 ± 0.00	0.635 ± 0.01	9.56 ± 0.20	9.98
	Bilayer	12.9 ± 0.44	0.954 ± 0.00	0.606 ± 0.01	7.45 ± 0.21	7.84
Light intensity	Active layer	J_{SC} [μA cm^{-2}]	V_{OC} [V]	FF	P_{max}[a)] [μW cm^{-2}]	Best P_{max}[a)] [μW cm^{-2}]
1000 lux	BHJ	105 ± 2.36	0.777 ± 0.01	0.634 ± 0.01	51.7 ± 1.44	54.6
	Bilayer	103 ± 2.33	0.835 ± 0.01	0.663 ± 0.02	57.2 ± 2.08	62.6

[a)]Due to difficulty of accurate PCE (P_{max}/P_{in}) calculation for indoor light, P_{max} was used to evaluate indoor device performance.

devices, as shown in Figure 2d (these values were extracted from Figure S9a, Supporting Information). The slope of bilayer devices (1.073 kT/q) is relatively close to kT/q compared to that of BHJ devices (1.285 kT/q). This indicates bilayer devices have lower trap-assisted recombination losses, consistently with device data showing much less V_{OC} reduction as well as higher FF under indoor light. In case of light intensity dependence on FF (Figure 2e), FF of bilayer devices are greatly enhanced with decreasing light intensity from 2500 to 500 lux of white LED. On the other hand, BHJ devices show similar or slightly higher FF under 500–1000 lux, but the values measured under 1000 to 2500 lux intensities are much lower than the FF measured under 1 Sun. The lowered FF can be seen more clearly in the *J–V* curves measured at different light intensities of the white LED. S-shaped *J–V* curves are observed in BHJ devices, especially at high indoor light intensity (Figure S10a, Supporting Information). Interestingly, bilayer devices do not show S-shaped *J–V* curves (Figure S10b, Supporting Information).

To understand the different trends of FF in both devices, shunt resistance (R_{sh}) is calculated from the *J–V* curves at different light intensities (Figure 2f). R_{sh} is known to be correlated with current losses in devices, originating from different parameters such as the edge of the cell, pinholes in the film, traps, or impurities.[24,25] A high R_{sh} is required to ensure good extraction of photo-generated charge carriers from the photoactive layer to the electrodes via a charge transport layer (i.e., HTL or ETL), especially for low-light or indoor light conditions.[6] Our devices show nearly identical dark *J–V* characteristics, so the different trends of R_{sh} originate from charge trapping rather than different physical characteristics such as edges, pinholes, or impurities. For BHJ devices, there is a greater decrease of R_{sh} as light intensity increases. For low intensity (500 to 1000 lux), R_{sh} of the BHJ is similar to the bilayer devices which can be attributed to less effect of trap-assisted or surface recombination losses under indoor light.[6,12,26] However, with increasing light intensity above 1000 lux, the R_{sh} values of BHJ devices decrease gradually leading to low FF, consistent with the S-shaped *J–V* curves. On the other hand, for bilayer devices, less dependence of R_{sh} on light intensity is observed and the R_{sh} values are high enough to minimize leakage currents, resulting in normal J-shaped *J–V* curves regardless of light intensity. Low R_{sh} of BHJ devices could be attributed to the significant recombination losses of BHJs due to undesirable isolated domain induced by nanostructured morphologies[27] and unfavorable interfacial contact between active layer and HTL or ETL.[24] These properties hinder the efficient charge transport and extraction in BHJ devices by lowering R_{sh} and FF. However, charge transport and extraction in bilayer devices are not significantly interrupted due to a more favorable morphology, that is, no isolated domains and desirable interfacial contact. High R_{sh} regardless of light intensity demonstrates the great applicability of bilayer OPVs to various indoor light intensity conditions.

The relationship between light intensity and J_{SC} is as expected, with J_{SC} showing a clear reduction at reduced light intensities due to lower charge generation. A slightly larger reduction of J_{SC} in BHJ devices is due to mismatch of absorption which can be explained by external quantum efficiency (EQE) spectra as shown in Figure S11, Supporting Information. In accordance with the absorbance spectra, BHJ devices exhibited higher EQE at a broader range of wavelengths, consistent with higher J_{SC} under 1 Sun. However, additional absorption originating from more aggregated IDIC in the BHJ cannot contribute to photocurrent generation under indoor light, due to lack of spectral overlap between the absorption and emission of the white LED. Whereas the narrower EQE of bilayer devices results in less wasted light absorption under LED illumination. Furthermore, it is known that J_{SC} follows a power law relationship with light intensity (I), namely $J_{SC} = I^{\alpha}$, where α determines the contribution of bimolecular recombination. As α is close to unity the contribution of bimolecular recombination becomes weeker.[23,28] In Figure S9c, Supporting Information, the slopes of J_{SC} versus I graph in log-log scale are almost identical in both BHJ and bilayer devices, indicating no significant differences in term of bimolecular recombination.

2.4. Light-Soaking Effect

In the previous section, S-shaped *J–V* curves of BHJ devices were observed more clearly than those of bilayer devices, as light intensity increased (Figure S10, Supporting Information). To find out the origin of the S-shape, we compare device performance measured before and after LS at 1 Sun for 2 min with the S-shape observed at a light intensity of 2500 lux (**Figure 3**). Surprisingly, *J–V* curves of BHJ devices recover to a normal J-shape after LS, resulting in improved FF and P_{max}. Bilayer devices also exhibit slightly enhanced FF and P_{max}, but the effect is less dramatic. OPV devices with ZnO ETL are known to require LS to obtain optimal device performance. Recent reports demonstrate that sub-gap trap/defect states of ZnO can be responsible for this LS effect.[4] The LS effect induced by sub-gap trap states can be more noticeable under indoor light conditions. Reducing energetic barriers at the interface between the photoactive layer and ZnO is also found to eliminate the S-shape and thus remove additional LS processes. In our devices as well, enhanced device performance of BHJs after LS could be attributed to the improved electronic properties of ZnO similar to previous reports,[4] since ZnO nanoparticles (NPs) were used as ETL in this work. In bilayer devices, on the other hand, LS is less effective due to better energetic matching at the interface between IDIC and ZnO NPs. Therefore, bilayer devices require no additional LS process.

We calculated series resistance (R_s) and R_{sh} from the *J–V* curves of Figure 3 before and after LS, as summarized in **Table 2**. R_s of both devices decreased after LS. This could be attributed to the reduced energetic barrier between active layer and ZnO NPs and improved electron transport ability of ZnO NPs by activating ZnO with 1 Sun LS.[4] For indoor OPVs, low leakage current is the most important prerequisite to obtain high efficiency, namely R_{sh} is more important than R_s. R_{sh} of bilayer devices was maintained with values of 48.0 and 42.4 kΩ cm^2, before and after LS, respectively. However, BHJ devices showed great differences in R_{sh} going from 16.0 kΩ cm^2 before to 45.1 kΩ cm^2, after LS. Low R_{sh} is related to recombination losses induced by isolated domains[27] or undesirable interfacial contact,[24] as we discussed in previous section. By comparing the LS effect, we identify that interfacial contact between the photoactive layer

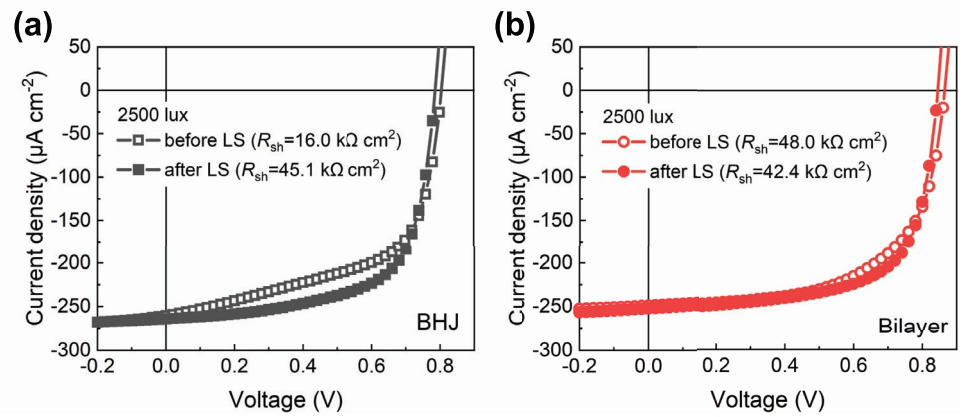

Figure 3. LS effect. *J–V* curves of a) BHJ and b) bilayer devices measured under 2500 lux (white LED), comparing before (open symbol) and after (solid symbol) LS under 1 Sun.

and ZnO charge transport layer is highly important to obtain high R_{sh}. Low R_{sh} before LS in BHJ devices can originate from unfavorable interfacial contact, as both donor and acceptor molecules are directly contacted to the ZnO NPs layer. This can be more noticeable in indoor light measurements, resulting in poor BHJ device performance without LS. On the other hand, only acceptor molecules are directly contacted to the ETL in bilayers, which is a more suitable structure in terms of electron transport and extraction. Hence, bilayer devices show good performance regardless of LS treatment, which is an important strength for indoor OPV applications.

2.5. Traps and Charge Extraction

To investigate the charge trapping effect in detail, surface photovoltage (SPV) was measured for BHJ and bilayer samples. SPV is a useful tool for characterizing charge accumulation and extraction properties by measuring changes in surface potential upon illumination, which can be induced by redistribution of photogenerated charge carriers within the active layer.[29–31] In this work, we use a quartz tungsten halogen lamp as excitation light source with an emission spectrum from 400 to 800 nm (Figure S12a, Supporting Information). The samples are prepared with a similar structure to OPV devices but without the top contact, Glass/ITO/PEDOT:PSS/active layer/ZnO NPs. First, SPV transients of the BHJ and bilayer samples are compared under 20 mW cm^{-2} illumination (**Figure 4**a). Positive SPV signal (Figure S12b, Supporting Information) indicates electron accumulation on the surface of the samples. The magnitude of SPV of the BHJ sample (492 meV) is higher than that of the bilayer (361 meV), indicative of the higher photocurrent generation in BHJs due to relatively larger heterointerface area. Despite a higher SPV magnitude in BHJs, SPV response speed to illumination is different compared to bilayers. In normalized SPV transients, it is clear that there are much faster turn-on and -off responses in bilayer samples, indicating efficient and fast electron extraction from active layer to the ETL without charge trapping. Conversely, the BHJ sample shows much slower turn-on and -off responses, producing long-lived turn-off signals. This indicates that the electron extraction process in BHJ devices is less efficient than in bilayers, possibly due to significant trapping of electrons at the non-ideal interfacial contacts (e.g., the polymer donor/ZnO) in BHJs.

Moreover, SPV transients were characterized under various light intensities (Figure 4b). Light intensities for SPV measurements were adjusted as 20.0, 9.10, 4.55, and 0.91 mW cm^{-2}, where estimated intensities in lux are 22 000, 10 000, 5000, and 1000 lux, respectively. To compare the changes of SPV magnitudes upon different light intensities, the graphs are normalized to the highest light intensity condition. Upon light intensity reduction, SPV magnitudes decrease in both BHJ and bilayer samples, which is expected from a lower number of photogenerated charge carriers. However, the reduction of SPV magnitudes of bilayer samples is much smaller than in BHJ, indicating more prominent recombination losses occurring in BHJs when the light intensity is decreased to 1000 lux, consistently with the higher V_{OC} and FF in bilayer devices discussed previously.[29,32] To further clarify the different trends of the SPV magnitude upon light intensity change, we plot normalized SPV magnitude versus logarithm of light intensity (Figure 4c). It is known that SPV magnitude is correlated with V_{OC} of OPV

Table 2. Summary of photovoltaic parameters of BHJ and bilayer OPV devices, measured under 2500 lux (LED), comparing LS effects.

Active Layer	LS	J_{SC} [μA cm^{-2}]	V_{OC} [V]	FF	P_{max} [μW cm^{-2}]	R_{sh} [kΩ cm^2]	R_s [Ω cm^2]
BHJ	Before	248 ± 6.97	0.805 ± 0.00	0.589 ± 0.00	118 ± 3.09	16.0	8.74
	After	250 ± 8.17	0.788 ± 0.00	0.649 ± 0.01	128 ± 5.08	45.1	4.14
Bilayer	Before	239 ± 6.24	0.865 ± 0.00	0.600 ± 0.01	124 ± 5.05	48.0	12.5
	After	240 ± 7.21	0.845 ± 0.00	0.650 ± 0.01	132 ± 5.81	42.4	8.24

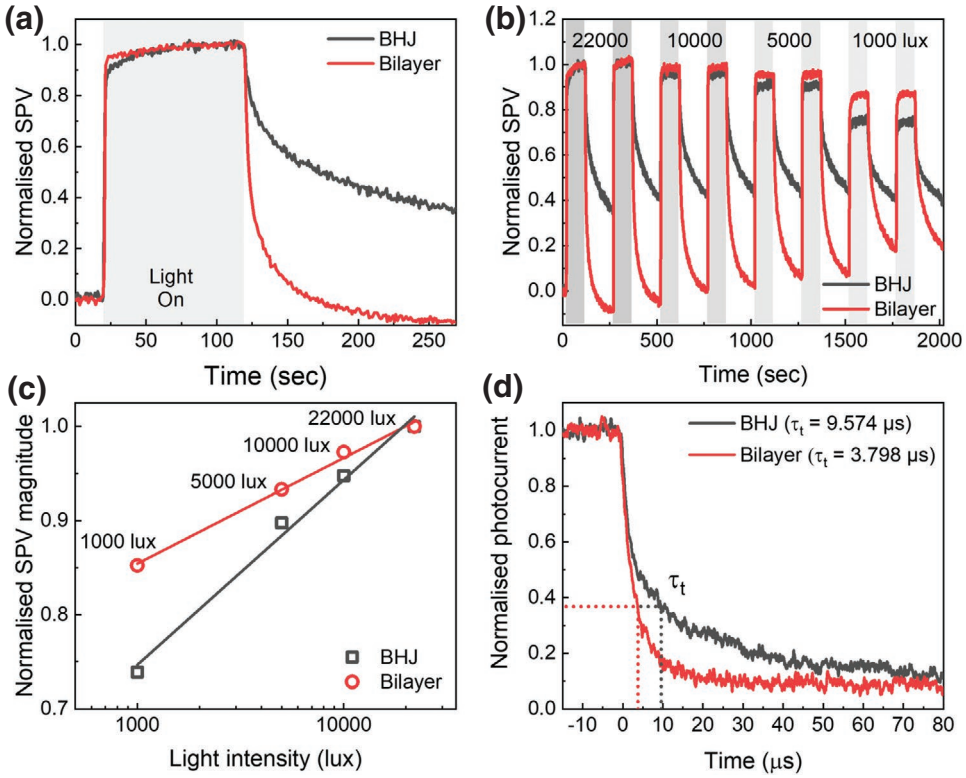

Figure 4. a) Normalized SPV measurements of BHJ and bilayer samples with structure of Glass/ITO/PEDOT:PSS/Active layer/ZnO NPs. b) Light intensity dependent normalized SPV measurements of BHJ and bilayer samples, and c) summary of SPV magnitude for each intensity. d) Photocurrent transients of the optimum BHJ and bilayer devices. Transport time (τ_t) is defined by the time when the initial signal drops to 1/e.

devices,[31] and both SPV and V_{OC} show excellent agreement with linear dependences on logarithm of light intensity. SPV changes are consistent with the V_{OC} changes upon light intensity change, which implies that V_{OC} losses of BHJ devices under indoor light can originate from significant trap concentration, leading to inefficient charge redistribution and extraction under illumination. On the contrary, the lower V_{OC} loss of bilayer devices can result from suppressed traps by minimized isolated domains as well as optimized interfacial contacts.

Transient photocurrent (TPC) decays were characterized at short-circuit conditions to compare charge extraction ability between BHJ and bilayer devices, as shown in Figure 4d. Non-normalized TPC data are shown in Figure S13, Supporting Information. Transport time (τ_t, defined by the time when the initial signal drops to 1/e) of bilayer devices (3.798 μs) is much faster than that of BHJ devices (9.574 μs). Less charge trapping of bilayer devices enables efficient charge extraction with reduced τ_t by a factor of 2.5 compared to the BHJ. Furthermore, hole and electron transport properties of BHJ and bilayer devices were evaluated by using space-charge limited current (SCLC) method, comparing them with neat PM6 and neat IDIC devices. Single carrier devices (hole- or electron-only) were fabricated and characterized as shown in Figure S14, Supporting Information. For single-carrier neat PM6 and IDIC devices, *J*–*V* characteristics show typical trap-free SCLC region at high voltages following Ohmic region at low voltages. Single-carrier bilayer devices also show Ohmic behavior followed by SCLC region without trap-filling limited current region, although it is not perfect single carrier diodes. In contrast, distinctive trap-limited SCLC and trap-filling limited current characteristics are observed in hole-only BHJ devices, indicative of significant hole trapping in the BHJs. By taking trap-filling limited voltage (V_{TFL} = 0.56 V) with assuming dielectric constant (ε_r) of BHJ film is 3, trap density is calculated to be 4.7×10^{17} cm^{-3} which is in a typical range (10^{16}–10^{18} cm^{-3}) value in NFA-based OPVs, although it is an order of magnitude higher than that of Y6-based BHJ devices (≈10^{16} cm^{-3}).[33] Interestingly BHJ devices show slightly higher hole mobility than that of neat PM6 devices possibly due to enhanced packing structure of PM6 in BHJ films, as evident in the absorption spectra (Figure 1c) showing prominent 0–0 PM6 peak in BHJ films. Electron-only BHJ devices do not show trap-filling limited current region, unlike hole-only BHJ devices. Molecular packing structure of high-crystalline NFAs cannot be easily disturbed by polymer, as other polymer:NFA systems also showed similar result of maintained electron transport properties regardless of blending with polymer.[33] This results also verify that bilayer structure is more suitable to obtain suppressed trap-assisted recombination, compared to those of BHJs.

2.6. Schematic Illustration of BHJ and Bilayer OPVs under Different Light Sources

Based on all the findings discussed herein, we propose a schematic illustration of the possible situation of BHJs and bilayers

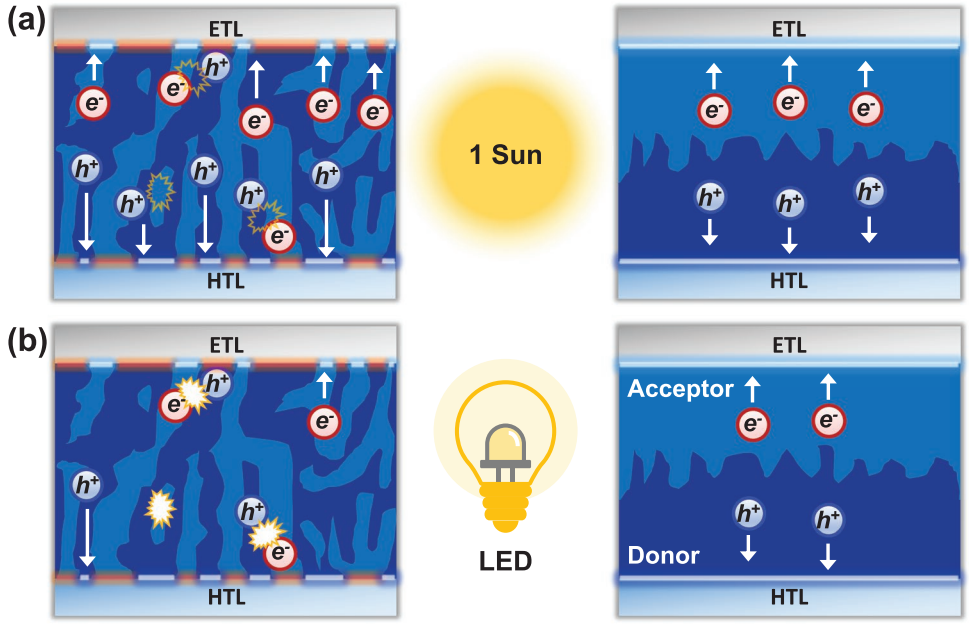

Figure 5. Schematic of transport and recombination of photogenerated charge carriers for BHJ and bilayer devices under a) 1 Sun and b) LED indoor light illumination. Exciton generation process is omitted. Dark blue and light blue color indicate donor and acceptor layers, respectively. Undesirable contacts between active layer and charge transport layers are indicated with red highlight in BHJ case.

during device operation under 1 Sun and indoor light (**Figure 5**). Structural properties of intermixed donor and acceptor molecules in BHJs are advantageous in terms of photocurrent generation, but undesirable traps induced by isolated domains and non-ideal interfacial contacts lead to inevitable recombination losses. For BHJ devices under high light, these traps rarely affect device performance. However, these recombination losses are not negligible under indoor light, consequently V_{OC} and FF are limited in BHJ devices. On the other hand, bilayers which simply consist of donor and acceptor layers are the optimum structure for charge transport and extraction with reduced intermixed donor/acceptor interfaces. Less domain boundaries can reduce traps and trap-assisted recombination, leading to much less V_{OC} loss under indoor light. In addition, the interfacial contact between photoactive layer and charge transport layers should be considered as an important factor to optimize R_{sh}. Thanks to the ideal contacts in bilayer devices as highlighted in Figure 5, charge carriers are effectively extracted to ETL and HTL by minimized recombination losses at the interface. As a result, high R_{sh} values are maintained under various intensity of indoor light and even without LS. This indicates that the bilayer strategy is an effective way to maintain high R_{sh}, which is an essential condition for indoor OPVs, and that bilayer OPV devices could be less sensitive to electronic properties of charge transport layers due to a more favorable energetic barrier alignment compared to those of BHJs.

3. Conclusion

In conclusion, we have successfully demonstrated the suitability of bilayer OPVs for efficient indoor light harvesting by identifying the key device parameters such as low recombination loss and high R_{sh} for indoor PV, which are satisfied by bilayer structures. Under 1 Sun, BHJ devices show better performance with higher J_{SC} and FF, compared to bilayer devices. However, under low indoor light intensities, the performance trends are reversed with bilayer devices exhibiting higher V_{OC} and FF, resulting in a higher P_{max} compared to BHJ devices. The light intensity dependence measurements show less dependence for the V_{OC} of bilayer devices than in BHJ devices, demonstrating strongly suppressed trap-assisted recombination in the bilayer. FF difference between bilayer and BHJ devices becomes more prominent at higher indoor light intensities and this is correlated well with the bilayer preserving a high R_{sh} in low light conditions, which is a crucial factor for indoor OPV performance. Additionally, high R_{sh} of bilayer devices enables excellent performances without the need for LS, whereas this was essential for BHJ devices. We attribute this to favorable interfacial contacts of bilayer devices having purer IDIC domains near the ETL and a smaller energetic barrier with deactivated ZnO. Finally, the reduced number of trap states in the bilayers is verified by SPV dynamics and TPC measurements showing faster and more efficient charge redistribution and extraction upon light illumination compared to those of BHJs. Our study demonstrates that inherent morphological defects induced by isolated donor and/or acceptor domains and non-ideal interfacial contacts in BHJ devices can inhibit device performance at indoor light conditions, and elimination of these morphological defects can be successfully attained by using a bilayer-structured active layer. This work suggests the great potential of bilayer OPV devices for indoor energy harvesting systems by demonstrating the importance of device architecture and interfacial structures of photoactive layers.

4. Experimental Section

General: PM6 and IDIC were purchased from Solarmer Materials. ZnO NPs were synthesized by following a reported literature.[34] Absorbance data were obtained using a Shimadzu UV-2550 UV–vis spectrophotometer. SPV and APS were measured by an APS04 Air Photoemission system (KP Technology) using a 2 mm gold tip in ambient conditions. AFM height images were obtained using a Park NX-10 AFM microscope in noncontact mode. The photocurrent transients were obtained with a DAQ card connected to a Tektronix TDS3032B Oscilloscope.

Device Fabrication Procedures and Characterization: OPV devices were prepared with a conventional structure of glass/indium tin oxide (ITO)/poly(3,4-ethylenedioxythiophene) polystyrene sulfonate (PEDOT:PSS)/active layer/ZnO NPs/Ag. Pre-patterned ITO on glass substrates were cleaned by ultra-sonication with deionized water, acetone, and 2-propanol. Then the substrates were dried in an oven at 80 °C overnight. PEDOT:PSS (Clevios, AI 4083) layers were spin coated on ITO substrates, and baked on a hot plate at 140 °C for 10 min in air. After baking, substrates were brought into a N_2 filled glove box. For BHJ devices, PM6:IDIC (1:1 w/w) blend solutions were prepared in chlorobenzene (CB) (26 mg mL^{-1}, total concentration) with 1 vol% of 1,8-octanedithiol (ODT). The solutions were stirred at 100 °C overnight prior to spin casting. After spin-coating the BHJ layer on top of the PEDOT:PSS substrates, the active layers were thermal-annealed at 100 °C for 5 min.

For bilayer devices, PM6 solutions were prepared in CB (10 mg mL^{-1}) with 1 vol% of ODT, and the solutions were stirred at 100 °C overnight. IDIC solutions were prepared in dichloromethane (9 mg mL^{-1}), and the solutions stirred at room temperature for 2 h before spin casting. PM6 layers were coated on top of the PEDOT:PSS coated substrates first, then the PM6-coated substrates were thermal-annealed at 100 °C for 5 min. Then IDIC layers were coated subsequently. By controlling concentrations and spin rates of solutions of PM6 and IDIC, thickness of PM6/IDIC bilayers were adjusted with 93 ± 2/50 ± 4, 60 ± 2/50 ± 4, 60 ± 2/72 ± 5, and 60 ± 2/103 ± 5 nm.

After spin-coating active layers, ZnO NPs (dispersed in methanol) were spin-coated. Then, the substrates were brought into a high vacuum chamber (≈10^{-6} Torr), and Ag (100 nm) was deposited by thermal evaporation. Device area was 4.5 mm^2. Measurements were conducted outside the glovebox, and the devices were stored in a nitrogen filled chamber. Solar simulator was used for 1 Sun measurement whose intensity was calibrated at 100 mW cm^{-2} with a standard silicon photodiode. LED light was used for indoor measurement whose intensity was calibrated with digital Luxmeter. *J–V* characteristics were measured with a Keithley 2400 source measurement unit. EQE was measured using an EQE system of a tungsten halogen lamp coupled with a grating spectrometer (CS260-RG-4-MT-D).

For single-carrier devices for SCLC measurements, hole-only devices were fabricated with a structure of ITO/PEDOT:PSS/Active Layer/MoOx/Ag. Electron-only devices were fabricated with a structure of ITO/ZnO/Active Layer/ZnO NPs/Ag. Thicknesses of neat PM6, neat IDIC, BHJ, and bilayer (PM6/IDIC) films for SCLC devices are 90, 90, 210, and 60/90 nm, respectively. Mobility is calculated using Mott–Gurney relationship and N_t is calculated using following equation: $N_t = \frac{2\varepsilon_0\varepsilon_r}{ed} V_{TFL}$, where ε_0 is vacuum permittivity, ε_r is dielectric constant, e is elementary charge, d is film thickness and V_{TFL} is trap-filling limited voltage.

Supporting Information

Supporting Information is available from the Wiley Online Library or from the author.

Acknowledgements

The authors thank Woojin Lee and Prof. Jin Young Kim (UNIST, South Korea) for the synthesis of ZnO nanoparticles. This research was supported by Basic Science Research Program through the National Research Foundation of Korea (NRF) funded by the Ministry of Education (2020R1A6A3A03039652). The authors also thank the UK EPSRC for the Plastic Electronics Centre for Doctoral Training (EP/L016702/1) and ATIP Programme Grant (EP/T028513/1), and the Global Research Laboratory Program of the National Research Foundation (NRF) funded by the Ministry of Science, ICT & Future Planning (NRF-2017K1A1A2 013153).

Conflict of Interest

The authors declare no conflict of interest.

Data Availability Statement

The data that support the findings of this study are available from the corresponding author upon reasonable request.

Keywords

organic solar cells, indoor organic photovoltaics, bilayer-heterojunction, bulk-heterojunction, light-soaking

Received: October 18, 2021
Revised: November 24, 2021
Published online: December 15, 2021

[1] a) Y. Cai, Y. Li, R. Wang, H. Wu, Z. Chen, J. Zhang, Z. Ma, X. Hao, Y. Zhao, C. Zhang, F. Huang, Y. Sun, *Adv. Mater.* **2021**, *33*, 2101733; b) F. Liu, L. Zhou, W. Liu, Z. Zhou, Q. Yue, W. Zheng, R. Sun, W. Liu, S. Xu, H. Fan, L. Feng, Y. Yi, W. Zhang, X. Zhu, *Adv. Mater.* **2021**, *33*, 2100830; c) J. Yuan, Y. Zhang, L. Zhou, G. Zhang, H.-L. Yip, T.-K. Lau, X. Lu, C. Zhu, H. Peng, P. A. Johnson, M. Leclerc, Y. Cao, J. Ulanski, Y. Li, Y. Zou, *Joule* **2019**, *3*, 1140; d) Y. Zeng, D. Li, Z. Xiao, H. Wu, Z. Chen, T. Hao, S. Xiong, Z. Ma, H. Zhu, L. Ding, Q. Bao, *Adv. Energy Mater.* **2021**, *11*, 2101338.

[2] a) Y. Xie, R. Xia, T. Li, L. Ye, X. Zhan, H.-L. Yip, Y. Sun, *Small Methods* **2019**, *3*, 1900424; b) J. Lee, H. Cha, H. Yao, J. Hou, Y.-H. Suh, S. Jeong, K. Lee, J. R. Durrant, *ACS Appl. Mater. Interfaces* **2020**, *12*, 32764.

[3] a) X. Li, R. Xia, K. Yan, J. Ren, H.-L. Yip, C.-Z. Li, H. Chen, *ACS Energy Lett.* **2020**, *5*, 3115; b) S. Song, H. W. Cho, J. Jeong, Y. J. Yoon, S. Y. Park, S. Song, B. H. Woo, Y. C. Jun, B. Walker, J. Y. Kim, *Sol. RRL* **2020**, *4*, 2000201; c) H. R. Yeom, S. Song, S. Y. Park, H. S. Ryu, J. W. Kim, J. Heo, H. W. Cho, B. Walker, S.-J. Ko, H. Y. Woo, J. Y. Kim, *Nano Energy* **2020**, *77*, 105146.

[4] J. Luke, L. Corrêa, J. Rodrigues, J. Martins, M. Daboczi, D. Bagnis, J.-S. Kim, *Adv. Energy Mater.* **2021**, *11*, 2003405.

[5] L.-K. Ma, Y. Chen, P. C. Y. Chow, G. Zhang, J. Huang, C. Ma, J. Zhang, H. Yin, A. M. Hong Cheung, K. S. Wong, S. K. So, H. Yan, *Joule* **2020**, *4*, 1486.

[6] S. Y. Park, Y. Li, J. Kim, T. H. Lee, B. Walker, H. Y. Woo, J. Y. Kim, *ACS Appl. Mater. Interfaces* **2018**, *10*, 3885.

[7] H. S. Ryu, S. Y. Park, T. H. Lee, J. Y. Kim, H. Y. Woo, *Nanoscale* **2020**, *12*, 5792.

[8] a) I. Mathews, S. N. Kantareddy, T. Buonassisi, I. M. Peters, *Joule* **2019**, *3*, 1415; b) V. Pecunia, L. G. Occhipinti, R. L. Z. Hoye, *Adv. Energy Mater.* **2021**, *11*, 2100698.

[9] L. Xie, W. Song, J. Ge, B. Tang, X. Zhang, T. Wu, Z. Ge, *Nano Energy* **2021**, *82*, 105770.

[10] M. Freunek, M. Freunek, L. M. Reindl, *IEEE J. Photovoltaics* **2013**, *3*, 59.
[11] C. M. Proctor, T.-Q. Nguyen, *Appl. Phys. Lett.* **2015**, *106*, 083301.
[12] S.-C. Shin, C. W. Koh, P. Vincent, J. S. Goo, J.-H. Bae, J.-J. Lee, C. Shin, H. Kim, H. Y. Woo, J. W. Shim, *Nano Energy* **2019**, *58*, 466.
[13] a) G. Yu, J. Gao, J. C. Hummelen, F. Wudl, A. J. Heeger, *Science* **1995**, *270*, 1789; b) A. J. Heeger, *Adv. Mater.* **2014**, *26*, 10; c) L. Dou, J. You, Z. Hong, Z. Xu, G. Li, R. A. Street, Y. Yang, *Adv. Mater.* **2013**, *25*, 6642; d) P. W. M. Blom, V. D. Mihailetchi, L. J. A. Koster, D. E. Markov, *Adv. Mater.* **2007**, *19*, 1551.
[14] a) H. Fu, W. Gao, Y. Li, F. Lin, X. Wu, J. H. Son, J. Luo, H. Y. Woo, Z. Zhu, A. K.-Y. Jen, *Small Methods* **2020**, *4*, 2000687; b) S. Dong, K. Zhang, B. Xie, J. Xiao, H.-L. Yip, H. Yan, F. Huang, Y. Cao, *Adv. Energy Mater.* **2019**, *9*, 1802832; c) L. Ye, Y. Xiong, Z. Chen, Q. Zhang, Z. Fei, R. Henry, M. Heeney, B. T. O'Connor, W. You, H. Ade, *Adv. Mater.* **2019**, *31*, 1808153; d) K. Jiang, J. Zhang, Z. Peng, F. Lin, S. Wu, Z. Li, Y. Chen, H. Yan, H. Ade, Z. Zhu, A. K.-Y. Jen, *Nat. Commun.* **2021**, *12*, 468.
[15] T. H. Lee, S. Y. Park, W.-W. Park, X. Du, J. H. Son, N. Li, O.-H. Kwon, H. Y. Woo, C. J. Brabec, J. Y. Kim, *ACS Energy Lett.* **2020**, *5*, 1628.
[16] S. Y. Park, S. Chandrabose, M. B. Price, H. S. Ryu, T. H. Lee, Y. S. Shin, Z. Wu, W. Lee, K. Chen, S. Dai, J. Zhu, P. Xue, X. Zhan, H. Y. Woo, J. Y. Kim, J. M. Hodgkiss, *Nano Energy* **2021**, *84*, 105924.
[17] T. H. Lee, S. Y. Park, X. Du, S. Park, K. Zhang, N. Li, S. Cho, C. J. Brabec, J. Y. Kim, *ACS Appl. Mater. Interfaces* **2020**, *12*, 55945.
[18] T. Wang, Z.-C. Wen, L.-H. Xu, C.-C. Qin, H. Yin, J.-Q. Liu, X.-T. Hao, *J. Mater. Chem. A* **2021**, *9*, 13515.
[19] M. Zhang, X. Guo, W. Ma, H. Ade, J. Hou, *Adv. Mater.* **2015**, *27*, 4655.
[20] Y. Lin, Q. He, F. Zhao, L. Huo, J. Mai, X. Lu, C.-J. Su, T. Li, J. Wang, J. Zhu, Y. Sun, C. Wang, X. Zhan, *J. Am. Chem. Soc.* **2016**, *138*, 2973.
[21] a) C. Labanti, M. J. Sung, J. Luke, S. Kwon, R. Kumar, J. Hong, J. Kim, A. A. Bakulin, S.-K. Kwon, Y.-H. Kim, J.-S. Kim, *ACS Nano* **2021**, *15*, 7700; b) J. Wu, J. Lee, Y.-C. Chin, H. Yao, H. Cha, J. Luke, J. Hou, J.-S. Kim, J. R. Durrant, *Energy Environ. Sci.* **2020**, *13*, 2422; c) J. Wu, J. Luke, H. K. H. Lee, P. Shakya Tuladhar, H. Cha, S.-Y. Jang, W. C. Tsoi, M. Heeney, H. Kang, K. Lee, T. Kirchartz, J.-S. Kim, J. R. Durrant, *Nat. Commun.* **2019**, *10*, 5159.
[22] Y. Li, Y. Lin, *J. Mater. Chem. C* **2021**, *9*, 11715.
[23] A. K. K. Kyaw, D. H. Wang, V. Gupta, W. L. Leong, L. Ke, G. C. Bazan, A. J. Heeger, *ACS Nano* **2013**, *7*, 4569.
[24] M.-S. Kim, B.-G. Kim, J. Kim, *ACS Appl. Mater. Interfaces* **2009**, *1*, 1264.
[25] B. Qi, J. Wang, *Phys. Chem. Chem. Phys.* **2013**, *15*, 8972.
[26] J. S. Goo, J.-H. Lee, S.-C. Shin, J.-S. Park, J. W. Shim, *J. Mater. Chem. A* **2018**, *6*, 23464.
[27] J. Wagner, M. Gruber, A. Hinderhofer, A. Wilke, B. Bröker, J. Frisch, P. Amsalem, A. Vollmer, A. Opitz, N. Koch, F. Schreiber, W. Brütting, *Adv. Funct. Mater.* **2010**, *20*, 4295.
[28] T. H. Lee, S. Y. Park, B. Walker, S.-J. Ko, J. Heo, H. Y. Woo, H. Choi, J. Y. Kim, *RSC Adv.* **2017**, *7*, 7476.
[29] M. Daboczi, I. Hamilton, S. Xu, J. Luke, S. Limbu, J. Lee, M. A. McLachlan, K. Lee, J. R. Durrant, I. D. Baikie, J.-S. Kim, *ACS Appl. Mater. Interfaces* **2019**, *11*, 46808.
[30] M. Chiesa, L. Bürgi, J.-S. Kim, R. Shikler, R. H. Friend, H. Sirringhaus, *Nano Lett.* **2005**, *5*, 559.
[31] Y.-J. Lee, J. Wang, J. W. P. Hsu, *Appl. Phys. Lett.* **2013**, *103*, 173302.
[32] M. Daboczi, J. Kim, J. Lee, H. Kang, I. Hamilton, C.-T. Lin, S. D. Dimitrov, M. A. McLachlan, K. Lee, J. R. Durrant, J.-S. Kim, *Adv. Funct. Mater.* **2020**, *30*, 2001482.
[33] Y. Zhang, G. Cai, Y. Li, Z. Zhang, T. Li, X. Zuo, X. Lu, Y. Lin, *Adv. Mater.* **2021**, *33*, 2008134.
[34] W. Lee, J. Yeop, J. Heo, Y. J. Yoon, S. Y. Park, J. Jeong, Y. S. Shin, J. W. Kim, N. G. An, D. S. Kim, J. Park, J. Y. Kim, *Sci. Rep.* **2020**, *10*, 18055.